Fingerprinting the α and γ phases of alumina using electron energy-loss spectroscopy

Capstone Project Research Paper

**Authors: David Cullen
Dr. Richard Vanfleet**

High Resolution Transmission Electron Microscopy Research Group

**Brigham Young University
Department of Physics and Astronomy**

March 28th, 2005
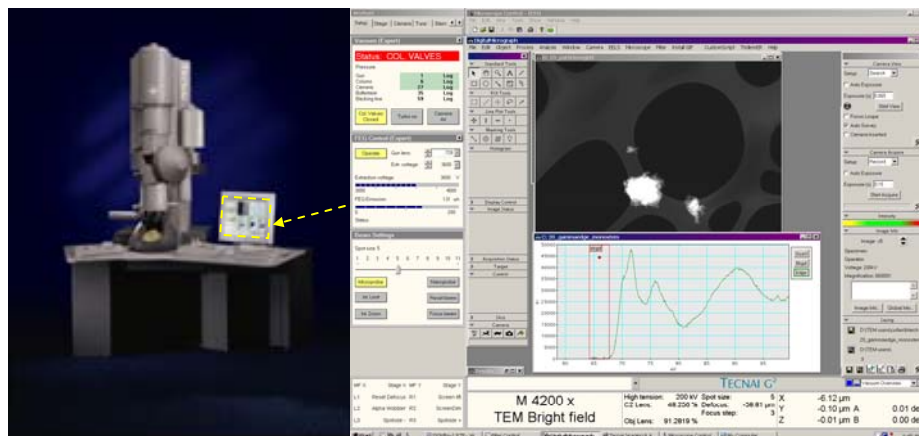
Abstract

The alpha and gamma phases of aluminum oxide were fingerprinted using electron energy-loss spectroscopy (EELS) with an energy resolution of 0.4 eV. Electron diffraction and powder x-ray diffraction were used to determine the phase of micron and nanopowder alumina samples. The results from indexing peak and ring diffraction patterns proved to be ambiguous and were resolved by comparing EELS spectra with published fingerprints. EELS spectra were generated from the powders with an energy resolution of 0.4 eV. This energy resolution was achieved using a Tecnai F20 Analytical Scanning Transmission Electron Microscope (STEM) equipped with a monochromator, Gatan energy filter (GIF) and high resolution spectrometer in STEM mode. These fingerprints are compared with published data and discrepancies between the spectra are discussed. The significance of using a monochromator with STEM mode for nanoparticle phase identification is addressed, followed by a brief roadmap delineating the goals of future EELS phase identification research.

Table of Contents

Introduction

Aluminum oxide (Al_2O_3) is the most widely used ceramic material and the second most abundant oxide in the earth's crust. It has a variety of industrial applications, especially in the fields of abrasives and wear resistant coatings. Commonly referred to as alumina, it can be found in seven different forms or phases, each having an identical stoichiometry, but different crystal structure and hence different mechanical properties. Six of the seven--chi (χ), eta (η), gamma (γ), kappa (κ), theta (θ), and delta (δ)--are known as the transition aluminas and form via a thermodynamic transformation sequence from the alumina hydroxide group.[1] The seventh phase, alpha (α) or corundum, is the only thermodynamically stable form, and can also be found in the precious gem form as ruby or sapphire. Most references to aluminum oxide or alumina refer to this seventh phase.

Because mechanical and crystal properties are phase dependent, certain phases find greater application in the industrial world. For example, the alpha, kappa, and gamma phases are widely used as resistant coatings in metal cutting tool applications.[2] Gamma alumina composite is also used in a special application as a heat insulator in the support structure of NASA's Wide-Field Infrared Explorer (WIRE) spacecraft.[3] Corundum, the most common form of alumina, finds an assortment of everyday applications ranging from high temperature crucibles to cosmetics. However, the other phases of alumina have yet to find their application in the industrial world.

Following the current trends of industrial materials research and development, alumina particle production is moving to the nanoscale. It is clear that efficient phase

characterization is an essential precursor to extensive application. As particle size moves

to the nanoscale, contemporary phase characterization techniques are quickly reaching

their limits of resolution. Single nanoparticle phase characterization is an important

companion to advances in nanoparticle production, and can be accomplished using high

resolution transmission electron microscopy (HRTEM). One application of HRTEM

implements a technique called electron-energy loss spectroscopy (EELS).

EELS commands a broad range of applications in materials analysis. In the

specific case of phase identification, the system can be used to generate a phase-

dependent energy-loss spectra which can be used as a type of fingerprint. EELS

fingerprints of α, κ, and γ alumina chemical vapor deposited (CVD) coatings were

published by Larson et. al. in 2000.[2] Their results--with an energy resolution of 0.6

eV--are presented in Figure 1.
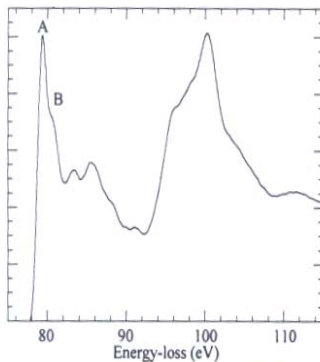
|		
Figure 1. Al L edge for α-Al$_2$O$_3$.	Figure 2. Al L edge for κ-Al$_2$O$_3$.	Figure 3. Al L edge for γ-Al$_2$O$_3$.
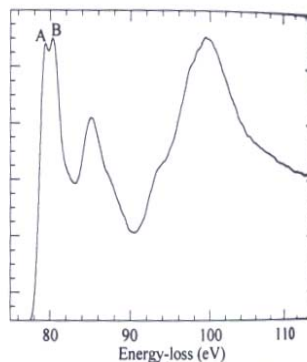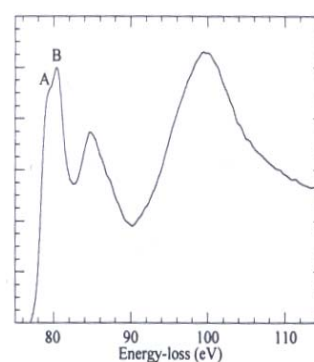
Figure 1:   EELS spectra of α, κ, and γ alumina CVD coatings taken with 0.6 eV energy resolution by Larson et. al. in 2000. The key distinguishing features of the fingerprints are the A and B peaks.[2]

These EELS fingerprints show the distinguishing features of α, κ, and γ alumina

energy spectra. The key features, labeled as peaks A and B, exist in the first primary

peak at around 80 eV and correspond to key differences in the crystal structure.

The major difference between the crystal structures of the gamma and alpha phases is attributed to the location and density of the aluminum atoms in tetrahedral and octahedral sites. Figure 2 shows the ABAB atomic layers of the alpha phase. The oxygen atoms form a hexagonal close packed (hcp) lattice. All aluminum atoms in the alpha phase are in octahedral sites, with 2/3 of the unit cell sites being filled. The unit cell is described as trigonal and belongs to the R-3c space group.[4,5]
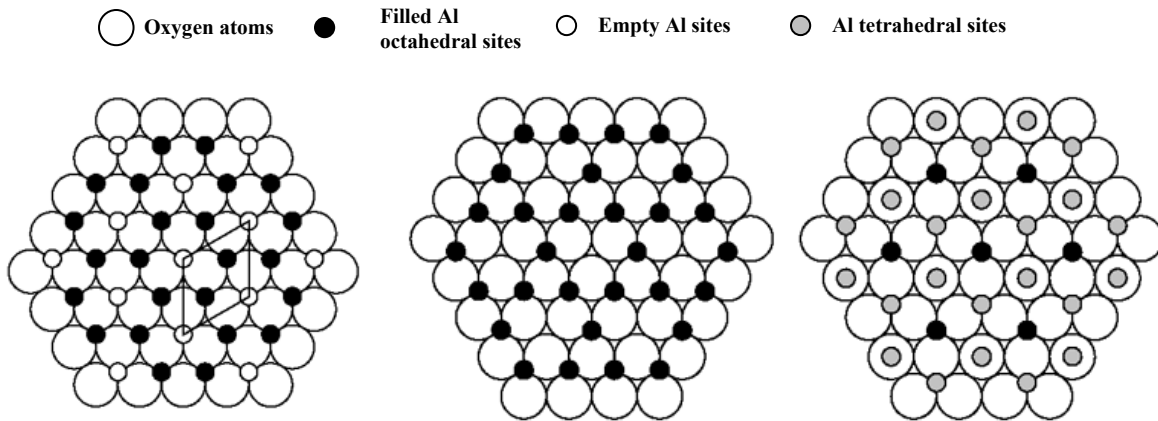

Figure 2: Repeating ABAB layers of aluminum and oxygen of the α-alumina crystal lattice. 2/3 of the aluminum octahedral sites are filled.[4]

Figure 3: Repeating ABC layers of the γ-alumina crystal lattice showing both octahedral and tetrahedral aluminum sites.[4]
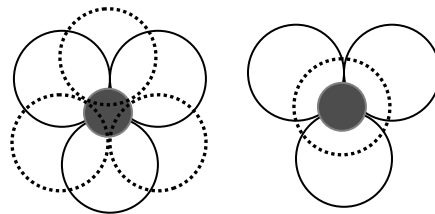
Figure 4: Examples of an octahedral site (left) and a tetrahedral site (right). The dotted circles correspond to overlying oxygen atoms

The exact structure of the gamma lattice, shown in Figure 3, is still unknown. The unit cell is defined as a defect spinel structure with 8 tetrahedral and 16 octaheral sites. It is described by an ABC stacking layer, with an A layer containing only octahedral sites and a C layer of both tetrahedral and octahedral sites. Although the location and

ratio of these sites is still under dispute, most sources agree that that the unit cell is face centered cubic (fcc) and belongs to the Fd-3m space group.[4,5]

It is suggested that the density of the octahedral and tetrahedral sites determines the relative locations of the A and B features in the primary peak of the alumina EELS spectrum.[2] Whatever the case, EELS phase identification rests on our ability to resolve these special features, which requires an energy resolution of less than 1 eV.

The scope of this project spans three major goals: first, to investigate how implementing an energy monochromator with EELS can improve energy resolution; second, to identify new features rising in the spectra at finer energy resolution; and, third, to demonstrate the capability of using scanning transmission electron microscopy (STEM) in tandem with the monochromator and EELS system to positively fingerprint single nanoparticles. As a matter of course, this paper briefly reviews the TEM sample preparation techniques used for this investigation, including wedge tripod polishing, dimpling, and powder sample preparation. This is followed by an explanation of electron diffraction as a tool for the phase identification of the alpha and gamma phases. Results of this analysis on nanopowders are presented in addition to results from x-ray powder spectroscopy. Finally, 0.4 eV energy resolution energy-loss spectra of the alpha and gamma phases of alumina, acquired using a unique HRTEM system which combines a state-of-the-art electron beam monochromator and EELS system, are presented and interpreted, followed by a discussion of important future EELS research.

Methods

Materials

The principle materials used in this analysis were micron and nanosized powders. A 60 nanometer γ aluminum oxide powder was purchased from Alfa Aesar, and a coarser grained, 60 micron γ aluminum oxide called CATALOX SBA-200 was donated by Dr. Calvin H Bartholomew of the BYU Chemical Engineering Department.

The polycrystalline α-alumina used in scanning electron microscopy (SEM) and electron diffraction came from an alumina crucible donated by Dr. Jeff Farrer of the BYU Physics Department.

Equipment and Software

This project utilized many types of equipment and computer software. The sample preparation stage required a slow speed diamond saw, polishing tripod, diamond lapping films, polishing wheel, 3mm ultrasonic disc cutter, dimpler, and precision-ion mill.

The microscopy part of the project utilized two transmission electron microscopes, a Tecnai F30 TEM and Tecnai F20 Analytical STEM equipped with a monochromator, GIF, and EELS system. Images and diffraction patterns were recorded on image plates and read out on a Ditabis laser drum scanner linked to Digital Micrograph imaging software, which was also used to index the diffraction patterns.

EELS spectra from the Tecnai F20 were also recorded and analyzed in Digital Micrograph. Further, an analysis on the grain size and orientation of the polycrystalline α-alumina was carried out using a Philips XL30 S-Feg SEM equipped with a backscattered electron detector.

Sample Preparation

We initially explored to two popular sample preparation techniques for this analysis. These processes are wedge tripod polishing and dimpling, which will be described briefly. Since TEM samples must be electron transparent—meaning a maximum thickness of 100 nanometers--these techniques require liberal quantities of time and patience. Fortunately, we located two sources of γ-alumina powder, and the previous techniques could be temporarily substituted for a much quicker process. These powders, identified in the materials section of this paper, were used for the TEM electron diffraction, x-ray powder diffraction (XPDS), and EELS investigations.

The first undertaking of this project was a joint effort with BYU student Jason Neff to produce a set of tripod polishers for the TEM specimen preparation lab. Computer generated instructions and diagrams of this process were adapted from a set of handwritten notes and are found in Appendix A. All materials--including aluminum, glass, Teflon, and micrometers--were provided by Dr. Vanfleet and machining was carried out in the Crabtree machine shop.

Samples for TEM and EELS analysis were initially designed to be wedge-type. A wedge sample demands many delicate hours of preparation, and, more often than not, ultimately ends in disaster. However, the product of a successful mechanical polish can provide an exceptionally thin edge for TEM analysis. The edge allows us to control thickness and crystal orientation during TEM operations, which are essential to obtaining clear and accurate diffraction patterns.

Since we were interested in understanding the average grain size and disorientation angles in the polycrystalline corundum, samples from the crucible were first prepared for an SEM analysis. Following the literature on OIM sample preparation, several specimens underwent a series of quick mechanical polishes with 15 micron to 1 micron lapping films and then ten minutes of ion milling.[6,7] Information concerning crystal size and orientation could then be obtained using an SEM capable of orientation imaging microscopy (OIM). An analysis of the effect of mechanical polishing on the specimen surface was also carried out in conjunction with this analysis.

Figure 5: Example of a wedge sample. The tip is polished to be electron transparent (<100 nm).

We confirmed that the material was polycrystalline with an average grain diameter of 200 microns. We feared that the large grains would rip out of the thin area of the wedge as we polished, leaving a thick, jagged edge instead of a thin, smooth area for analysis. For this reason, the wedge technique was temporarily abandoned.

We next worked towards preparing samples using a dimpling technique. This began by cutting small sections from the polycrystalline crucible using a low speed diamond wheel saw. The faces were polished flat using a tripod polisher and 30 micron

diamond lapping films. Three millimeter discs were then cut from these sections using a

Gatan Ultrasonic Disc Cutter. Typically, the desired specimen thickness before dimpling

is between 80 and 100 microns. However, considering the brittleness of the material and

hoping to maintain a greater level of structural integrity, the initial disc samples were

only polished down to a thickness of between 150 and 200 microns. However, as we will

show, these samples would prove to be incompatible with the low-angle ion mill.

The thinned 3 mm discs were dimpled using a Gatan dimpler with 15 diameter

copper and felt discs embedded with polycrystalline diamond compounds ranging from

15 to 0.25 microns. It was intended that the final thickness at the center of the dimple

range between 15 and 30 microns. The sample was then placed in a precision ion

polishing system (PIPS), which employs ionized argon atoms to mill the center of the

specimen until perforation, leaving an electron transparent region around the small hole

for TEM analysis. At this stage, however, it was discovered that because of the

nonadjustable low angle of the ion-mill, samples edge thickness needed to be polished to

below 100 microns for the mill to be effective.
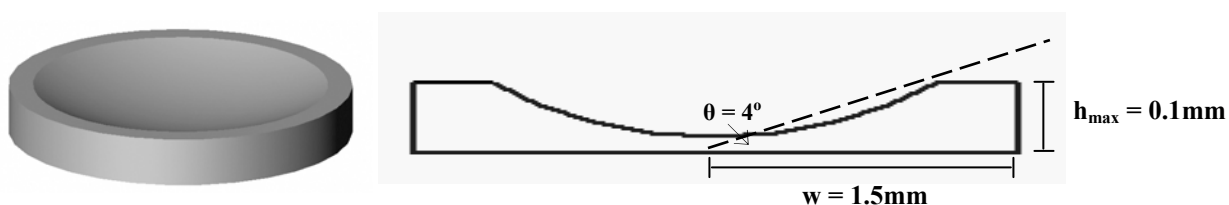
Figure 6: **(Left) An example of a 3 mm dimpled disc.**
(Right) Trajectory of PIPS ion beam incident at 4 degrees. The
maximum allowable height of the sample's edge is ≈ 100 microns

Fortunately, we discovered an on-campus source of micron-sized gamma alumina powder and later were able to purchase nanosized powders of the same phase. Sample preparation for powders is a very simple process of applying a small quantity of powder on to a lacy carbon grid.

There are several disadvantages to using powders, however. Powders tend to clump together, forming sections of varying crystal orientation, thickness, and, as we would soon discover, composition. Single particle isolation can be very difficult. Fortunately, these powders proved to be excellent samples. A small amount of powder was sprinkled on a three millimeter lacy carbon film, which could be immediately inserted into the microscope for analysis.

Electron Diffraction

Once a sample was prepared for TEM analysis, its phase was confirmed using electron diffraction. The diffraction mode utilizes the electrons diffracted by the atomic planes of the crystal. Information concerning atomic spacing and crystal structure can be harvested from the images by a process called indexing.

Diffraction from a single, uniform crystal forms a series of peaks called a spot diffraction pattern, while polycrystalline and amorphous materials will scatter electrons to form continuous rings.

A typical TEM diffraction image of silicon is shown in Figure 7. The number of pixels between diffraction peaks can be determined using the image processing software. This value is proportional to the spacing between planes, known as the *d*-spacing. Each crystal structure has a unique set of *d*-spacings, and the type and phase of a material can be determined by comparing *d*-spacings calculated from the pattern to those in published data tables.

$$\text{(1)} \quad L\lambda = Rd$$

L = camera length
λ = electron wavelength
R = horizontal distance
d = d spacing

$$\text{(2)} \quad d = \frac{1}{(k)(\#pixels)}$$

$$\text{(3)} \quad k = \frac{R}{(L)(\lambda)(\#pixels)}$$
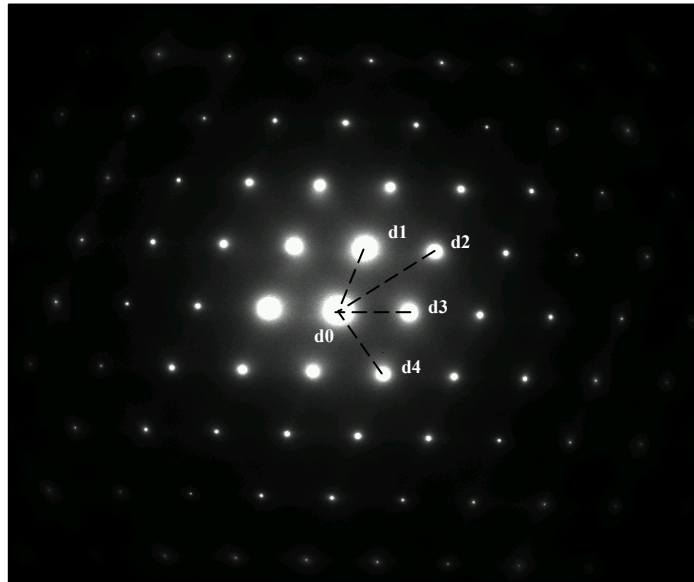
Figure 7: TEM electron diffraction pattern of silicon taken at a 930 mm camera length. The pattern was indexed and used to determine the proportionality constant *k*.

Equation (1) is a result of the Bragg Equation under the small angle approximation. In this paper, the proportionality constant connecting real and pixel space will be denoted by *k*, and has units of Å^{-1}/pixels. This constant is dependent on the camera length and can be calculated in two ways. The first method implements Equations (1) through (3) and will hence be called the Bragg method.

The wavelength (λ) is computed using the relativistic momentum, as shown in Equations (4)-(8), where *V* is the accelerating voltage, *h* is Plank's constant, *e* is the charge of an electron, *c* the speed of light, and m_o is the rest mass of an electron.

$$(4) \ E \ = E_o + U \ = \ m_o c^2 + (eV)$$

$$(5) \ E^2 = (m_o c^2)^2 + (pc)^2$$

$$(6) \ p = \frac{(E^2 - m_o^2 c^4)^{1/2}}{c}$$

$$p = \frac{(eV(eV + 2m_o c^2))^{1/2}}{c}$$

$$p = \left[2m_o eV (1 + \frac{eV}{2m_o c^2}) \right]^{1/2}$$

$$(7) \ \lambda = h/p$$

$$(8) \ \lambda = \frac{h}{\left[2m_o eV (1 + \frac{eV}{2m_o c^2}) \right]^{1/2}} \approx 1.968 \ pm$$

The second method for computing the proportionality constant (*k*) utilizes a direct comparison of pixel spacing to theoretical *d*-spacings and hereon will be referred to as the method of ratios. As an example, silicon is a cubic lattice with a lattice parameter (*a*) of 5.42 Å.[8] The *d*-spacings in silicon can be calculated by inserting integer values for the miller indices (*j, k, l*) into the *d*-spacing formula for a cubic lattice, given by Equation (9).

$$(9) \ d = \frac{a}{\left[j^2 + k^2 + l^2 \right]^{1/2}}$$

Ratios of these theoretical *d*-spacings computed from Equation (9) are then compared to ratios of the pixel spacings. The value of *k* can then be determined by multiplying the appropriate theoretical *d*-spacing with its corresponding value in pixel space, as shown by Equation (10).

$$(10) \quad k = \frac{1}{(d_{theor})(\#pixels)}$$

	# pixels	ratio: d_1/d_x	(j,k,l)	d_{theor} (Å)	ratio: $d_{(j,k,l)}/d_{(1,1,1)}$
d1	405.3250	1.0000	(1,1,1)	3.1356	1.0000
d2	660.7600	0.6134	(2,2,0)	1.9201	0.6124
d3	404.0889	1.0031	(1,1,-1)	3.1356	1.0000
d4	469.8250	0.8627	(0,0,2)	2.7155	0.8660

Table 1: Method of ratios used on a silicon diffraction pattern (Figure X) used to determine the value of k ($\approx$7.87e-4 Å^{-1}/pixel).

By comparing the ratios in Table 1, it can be seen that peaks d1 and d3 from Figure 7 correspond to the $(1,1,\pm1)$ plane, peak d2 to the (2,2,0) plane, and peak d4 to the (0,0,2) plane. Inserting the paired values into Equation (10) yields an averaged value for k of 7.87e-4 Å^{-1}/pixel. This method was used on diffraction patterns from silicon, corundum, and platinum to calculate the proportionality constant.

X-Ray Powder Diffraction

The powder purchased from Alpha-Aesar was analyzed using x-ray powder diffraction by Dr. Dana Griffen of the BYU geology department to confirm the presence of both α and γ alumina. Since electron diffraction analysis indicated the presence of two phases of alumina in the γ-alumina nanopowder, this technique was used to confirm this surprising result.

EELS

After the phase confirmation stage was completed, samples were analyzed using electron-energy loss spectroscopy. When the electron beam passes through a material, the beam electrons transfer energy to the electrons in the sample via inelastic scattering.

These excited electrons in turn emit that energy in different forms, such as x-rays, auger electrons, and secondary electrons, which can all be analyzed to extract information about the specimen. EELS is an analysis of the transmitted beam electrons, and thus is a direct measurement of the energy transfer to the material. Specifically, we used EELS to measure the energy lost due to inner shell excitation, or the transfer of energy to the electrons in the inner shells of the atoms. The number of electrons (counts) detected is plotted verses electron energy loss to create an energy spectrum containing peaks corresponding to the ionization energy of the inner shell.[10] A typical spectrum is shown in Figure 8.

The background noise can be subtracted from the spectra to form more distinct peaks. The peaks seen in Figures 8 through 10 correspond to L_3-shell transitions of the aluminum atoms, which is the $2P^{3/2}$ level of electrons. The location and shape of the peak is used to determine the composition and specific phase of the specimen.
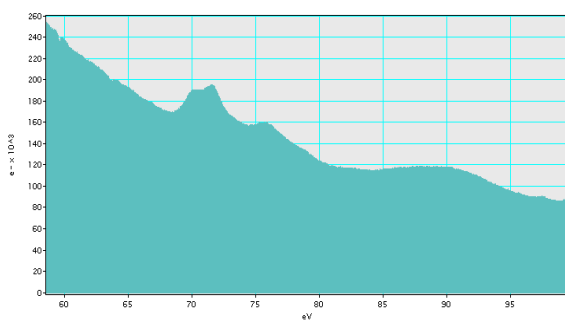
Figure 8: EELS spectra of γ-alumina without background subtraction
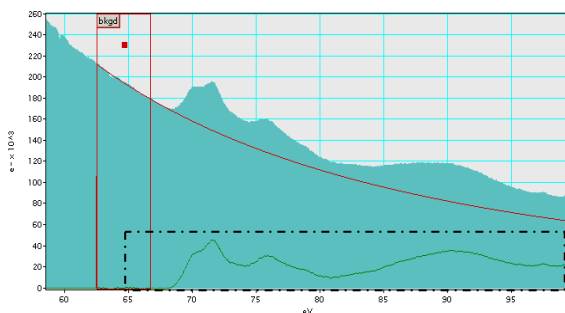
**Figure 9: EELS spectra of γ-alumina showing fit for background subtraction.**
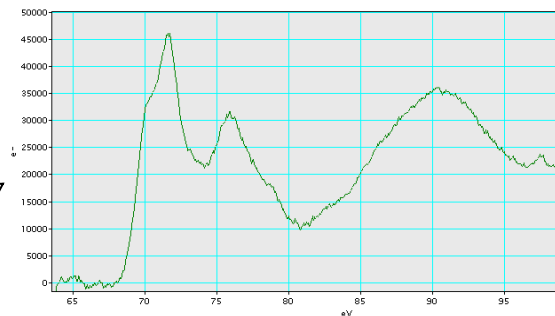
Figure 10: EELS spectra of γ-alumina after background subtraction

The energy resolution is determined by taking the full width at half maximum (FWHM) of the zero loss peak. The eV axis can be calibrated by setting the center of the zero loss to 0 eV, but because the axis of the spectrum is continuously shifting during analysis, we also took spectra of the carbon grid to determine the offset of the alumina spectra. We expect the edge of the gamma and alpha alumina spectra to fall at about 78 eV.[10]

Results

Sample Preparation

The powders sprinkled on a lacy carbon grid proved worthy of TEM analysis and were used for electron diffraction, x-ray powder diffraction, and EELS. Figure 11 shows both optical and TEM images of these lacy grids. A holey carbon film is laid over a copper grid and the nanopowders that are sprinkled onto the gird bind to the lacy carbon film.
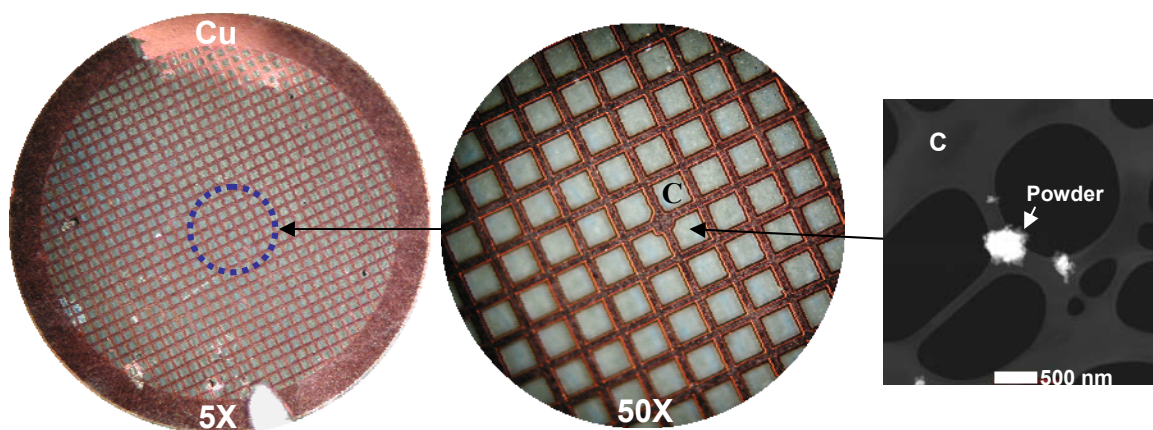
**Figure 11: Images of a lacy carbon grid taken with an optical light microscope
and TEM. A holy carbon film is suspended over a copper gird (left and middle).
A fine powder is sprinkled onto the gird and nanoparticles are trapped on the
carbon film (right).**

A wedge sample of alpha alumina was also used in the initial stages of the project as a standard to determine the proportionality factor k. As previously stated, it was determined that before dimpling and ion-milling, 3mm discs need to be polished to a thickness of less than 100 microns.

OIM on polycrystalline α-alumina

OIM analysis showed that most grain sizes in our polycrystalline α-alumina sample ranged between 150 and 300 microns. Although this grain size provides an excellent cross section for EELS analysis, it did bring up concerns with sample preparation, which are yet to be completely resolved. A complete report of this OIM analysis can be found in an unpublished personal paper by the author entitled "Orientation Image Microscopy of Alpha Alumina."   Some of the results of this analysis are shown in Figures 12(a) and 12(b). Data from this paper will be useful for future studies which will implement this polycrystalline material.


Figure 12(a): Grain map of polycrystalline α-alumina generated using a SEM equipped with OIM .
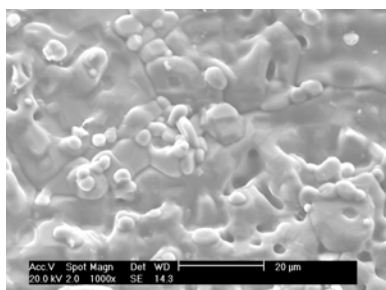
Unprepared surface of alpha alumina
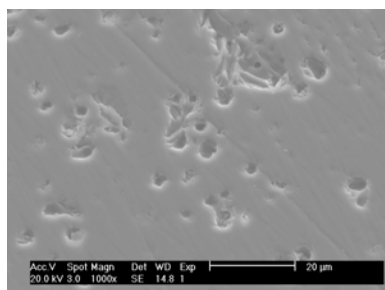
Surface prepared alpha alumina with 15 μm polish
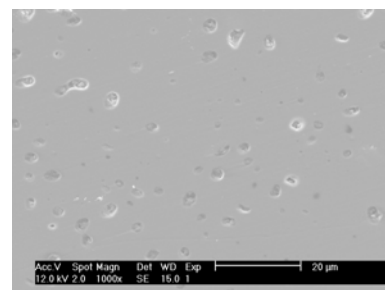
**Surface prepared alpha alumina with 1 μm polish**

Figure 12(b): SEM images of the surface of sections of polycrystalline α-alumina sample taken from a crucible

Electron Diffraction

Electron diffraction patterns of alpha and gamma alumina, platinum, and silicon were recorded on image plates at a camera length of 930 mm. Samples of platinum, silicon, and α-alumina were used to determine the value of k. Figure 13 shows an indexed diffraction pattern of α-alumina used to calculate an average value for k. Four peaks were indexed using the method of ratios, then Equation (10) was used to determine the value of k for each spacing. An average of these four values yielded a k value of 8.01e-4 $\pm$ 0.03e-4 Å⁻¹/pixel.

Table 3 gives the other values of k calculated from the diffraction patterns of the other materials using both the Bragg method (Method 1) and the method of ratios (Method 2).

Figure 13: Diffraction pattern from wedged α-alumina sample used to determine the multiplier k used in d-spacing calculations. The (h,k,l) plane corresponding to each peak were determined by the method of ratios (2).
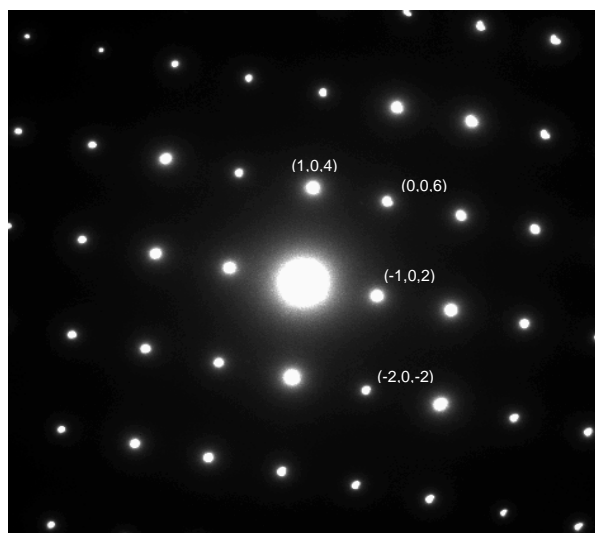
(h,k,l)	$d_{(pix)}$	$d_{(theor)}$ (Å)	k (Å⁻¹/pixel)
(-1,0,2)	358.5	3.479	8.0178E-04
(1,0,4)	491.11	2.552	7.9789E-04
(2,0,2)	635	1.964	8.0183E-04
(0,0,6)	574.46	2.165	8.0405E-04
		Average:	8.0139E-04
		Stnd Dev:	2.56265E-06

Table 2: Calculation of k using data taken from Figure 13

Table 3: Experimental values of k calculated from the diffraction patterns off various materials

Material	Method	k (Å⁻¹/pixel)	Stnd Dev.
α-Alumina	2	8.0139E-04	2.60E-06
Silicon	2	7.8701E-04	2.30E-06
Silicon	1	8.1927E-04	--
Platinum	2	7.7900E-04	2.60E-06
Average		7.9667E-04	
Stnd Dev		1.77E-05	

As seen in Table 3, the average value of k calculated from these different materials is 8.0e-4 $\pm$ .2e-4 Å^{-1}/pixel. This value was used to determine the d-spacings in later diffraction patterns to a rather remarkable degree of accuracy.

From Equations (1)-(3), we note that the proportionality constant is a function of camera length. Using the platinum standard, nine diffraction patterns were taken at camera lengths from 0.190 m to 1.9 m. The values of k calculated from these patterns were plotted against working distance to get Equation (12) with an R^2 value of 0.997. Figure 14 shows a plot of this fit along side the theoretical curve derived from Equation (3). These equations can be used to determine an approximate value of k for any working distance.

$$(11) \quad k_{theor} = \alpha R(L\lambda)^{-1}$$

$$(12) \quad k_{exp} = .8496 * L^{-1.0226}$$
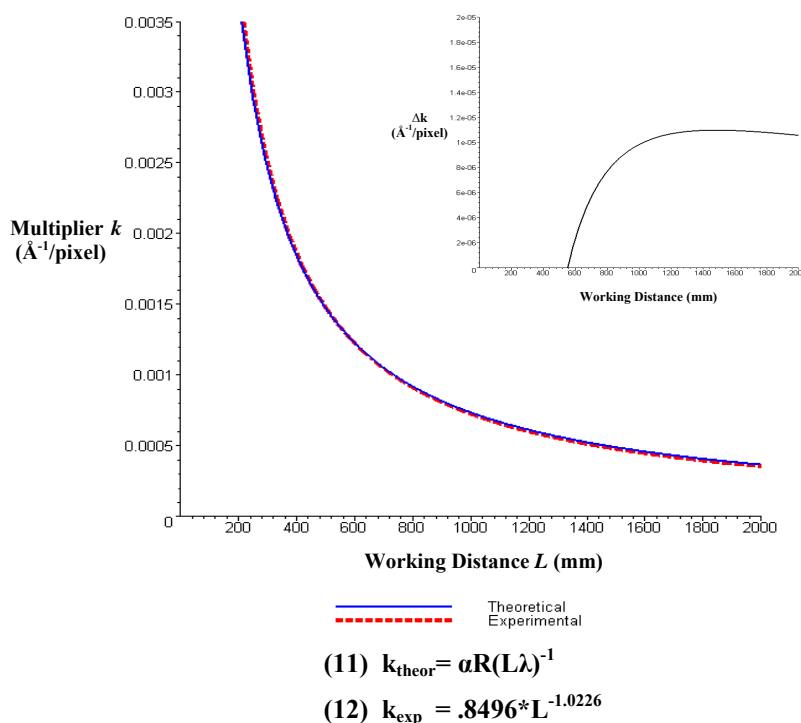
Figure 14: Comparison of theoretical and experimental curves for determining the proportionally constant used in relating distance in image-space (pixels) of diffraction patterns recorded on image plates and real space (Å). The experimental curve resulted from a fit to 9 different working distances using diffraction from a platinum crystal. Values for k were computed using Method 2 . Platinum has an fcc lattice, and theoretical d-spacings can be easily calculated using equation where a=3.9321 Å. k_{theor} (11) is a result of eq. (1)-(3),where α=1e-7, R=14.5, λ=1.968 ρm.

Also displayed in Figure 14 is a plot of the difference between k_{theor} and k_{exp}. As camera length increases, the two curves begin to diverge. The maximum difference between the curves is about 1.2e-05 Å^{-1}/pixel at a camera length near 1.5 m. This is roughly a 2% difference, which, for most calculations, is an acceptable degree of error.

Having thus determined the value of the multiplier, we were able to correctly index diffraction patterns from the γ-alumina powders and confirm the phase of our samples. The diffraction analysis was first carried out on the 60 nanometer γ-alumina powder. We observed two types of crystal structures; what appeared to be fine-grained or amorphous chunks and larger, single crystalline grains (see Figure 17). We begin with the evaluation of the diffraction pattern from the larger, single grain crystals. Although the nanopowder was supposed to be uniform gamma alumina, these patterns were identified as those belonging to α-alumina.

Figure 15: Indexed diffraction patterns of α-alumina
taken at a working distance of 930 mm
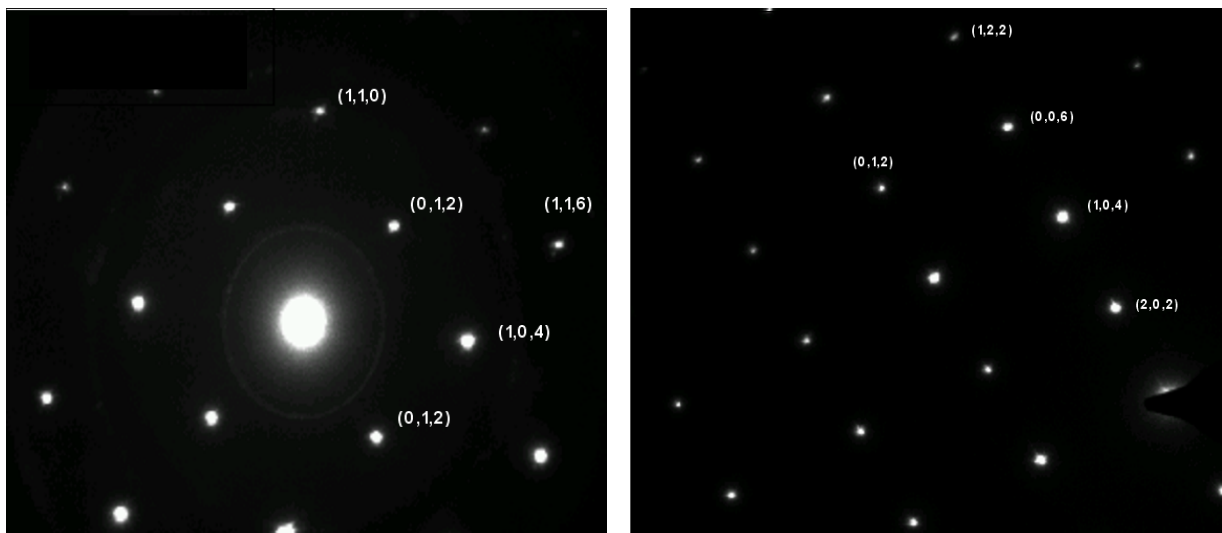
(h,k,l)	pixels	d_{calc}	d_{theor}	%diff
(1,1,0)	519.00	2.404	2.379	1.06
(0,1,2)	353.93	3.526	3.479	1.34
(1,1,6)	768.75	1.623	1.601	1.39
(1,0,4)	483.60	2.580	2.552	1.11
(0,1,2)	352.20	3.543	3.479	1.84

Table 4

(h,k,l)	pixels	d_{calc}	d_{theor}	%diff
(1,0,2)	358.10	3.485	3.479	0.16
(-1,0,4)	490.55	2.544	2.552	-0.32
(0,0,6)	574.07	2.174	2.165	0.4
(-2,0,2)	633.43	1.970	1.964	0.3
(1,2,2)	825.70	1.511	1.514	-0.18

Table 5

Figure 15 shows two such diffraction patterns with the accompanying diffraction data contained in Tables 4 and 5. The column labeled [%diff] gives the percent difference between the measured and theoretical values.

As expected, the second type of material turned out to be agglomerated chunks of gamma nanocrystals. Because of the ultra fine nature of the gamma powder, the electron beam simultaneously diffracted through multiple gamma crystals at different orientations. This lead to a diffraction pattern comprised of rings. By determining the spacing between the center of the pattern to the center of the ring, we were able to match these rings to the (4,0,0) and (4,4,0) planes of gamma alumina.
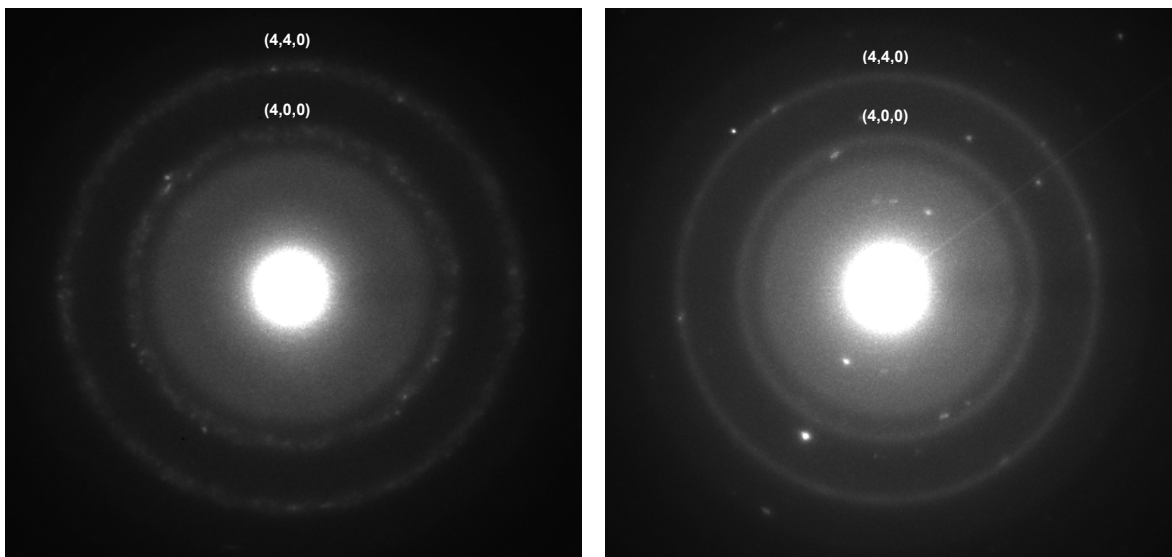
Figure 16: Diffraction rings from gamma alumina. The pattern is amorphous-like because the electrons are scattered by numerous, very fine gamma particules. The left was taken from samples donated by the chemical engineering department and the right from the sample from Alfa Aesar. It appears some diffraction peaks from the large alpha crystal interspersed among the gamma.

It is important to the note that we were only able to confidently characterize the nanocrystals after having compared our EELS spectra to the Larson et. al. published fingerprints. Table 6 demontsrates this point. In comparing the data to different phases of alumina and silicon--small grains of silicon were also found among the grains of alumina-- we see, based on the percent difference between the theoretical and calcualted values, that κ-

Unknown	# pixel	d_{calc}	
Ring 1	599	2.0406	
Ring 2	855.5	1.4376	

gamma	hkl	d_{theor}	%diff
Ring 1	4,0,0	1.997	2.18
Ring 2	4,4,0	1.395	3.05
alpha	hkl	d_{theor}	%diff
Ring 1	1,1,3	2.085	-2.13
Ring 2	1,2,4	1.404	2.39
silicon	hkl	d_{theor}	%diff
Ring 1	2,2,0	1.92	6.28
Ring 2	2,1,3	1.451	-0.92
kappa	hkl	d_{theor}	%diff
Ring 1	2,1,2	2.06	-0.94
Ring 2	1,1,4	1.45	-0.86

Table 6: Attempts to fit different ceramics to the data from Figure 16. The material is nominally gamma alumina, but the results from the electron diffraction analysis make it difficult to determine the actual phase of the alumina sample.

alumina actual provides the best fit to the data, followed by α-alumina. The gamma phase comes in at third, just edging out silicon. Thus we see how difficult it can be to accuratly and confidently characterize nanoparticles using convential methods.

In summary, we discovered the 60 nanometer powder contained two phases of alumina: a fine-grained gamma phase and a larger single-crystal alpha phase, as shown in Figure 17.   This proved to be convenient for the EELS analysis, in that we could analyze both phases in one sample.
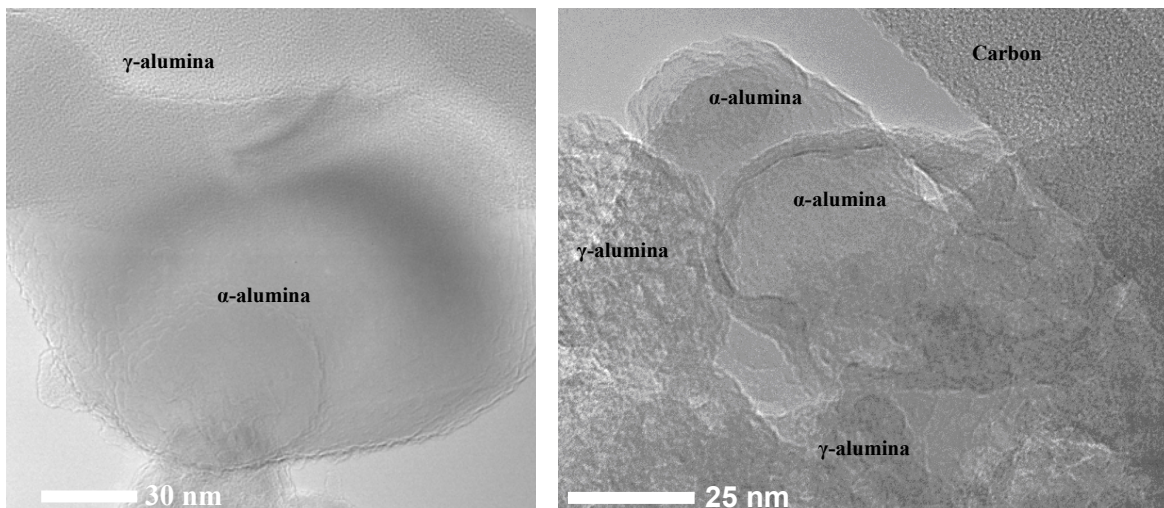

**Figure 17: Bright field TEM image of alpha and gamma alumina particles.
The alpha phase appears as the larger single crystals while the gamma phase
appears as an amorphous-like strucutre**

X-Ray Powder Diffraction

The results of x-ray diffraction performed by Dr. Dana Griffen confirm that the nanopowder from Alpha Aesar contains both alpha and gamma phase alumina. We note how the gamma peaks appear diffuse in comparison to the sharper alpha peaks, suggesting that the single crystallites are indeed α-alumina


Figure 18: X-ray powder diffraction data confirming the presence of alpha and gamma alumina in the Alfa Aesar 60 nm powder.

and the fine-crystalline nanoparticles are γ-alumina.

Electron Energy Loss Spectroscopy

After the diffraction analysis was completed, both sets of powders were studied via electron energy loss spectroscopy and energy spectra for α-alumina and γ-alumina were collected with 0.4 eV energy resolution. Spectra were taken via the Tecnai F20 TEM in imaging, diffraction, and scanning mode. The spectra shown hereafter were taken with the microscope in scanning mode (STEM), which provided the cleanest spectra of the three modes.

Determining Resolution and Offset

The energy resolution was determined by taking the full width of the zero-loss peak at half its maximum (FWHM). The zero-loss peak is generated by the beam

electrons that have no interaction with or elastically scatter from the sample. As

expected, we achieved the best resolution by running the monochromator in conjunction

with the Gatan energy filter (GIF) and EELS system in STEM mode. Figure 19 shows a

typical zero-loss peak with a FWHM value of
roughly 0.4 eV.

We note the -1.5 eV offset of the zero loss

peak.   This axis must be continually recalibrated

because it is offset every time we move the beam

and shifts spontaneously due to drifting in the

detector. Usually, we set the eV axis to read zero

at the center of the zero-loss peak, but since we

increase the beam intensity to maximize the

number of counts when resolving the aluminum

peak, we can't allow the highly intense zero loss

peak to simultaneously strike the detector for fear

of causing permanent damage to the sensitive

phosphor.

Figure 19: (Top) Zero-loss peak used to determine energy resolution. The energy resolution is the full width at half max (FWHM) of the peak (0.4 eV), (Bottom) EELS spectrum of carbon, which can be sued to calibrate the eV axis

As previously explained, an alternate form

of calibration can be done by taking an energy

spectrum of the carbon film to determine the proper offset. Figure 19 shows a carbon

peak taken while doing EELS on the uniform gamma alumina powder. The first carbon

peak should fall at 284 eV, but from the spectrum in Figure 19 we see that this peak is

offset by about 8 eV. Thus, the EELS spectra that were taken just before or after the

carbon peak was resolved would be offset by roughly that value. However, we did not go to the trouble of constantly calibrating the eV axis since the principle objective of this investigation was to resolve the features in the primary aluminum peak.

Figures 20 and 21 are EELS spectra of gamma and alpha alumina taken with a resolution of 0.4 eV. With this resolution, we can easily distinguish between the two phases according to the location and relative height of the A and B peaks.
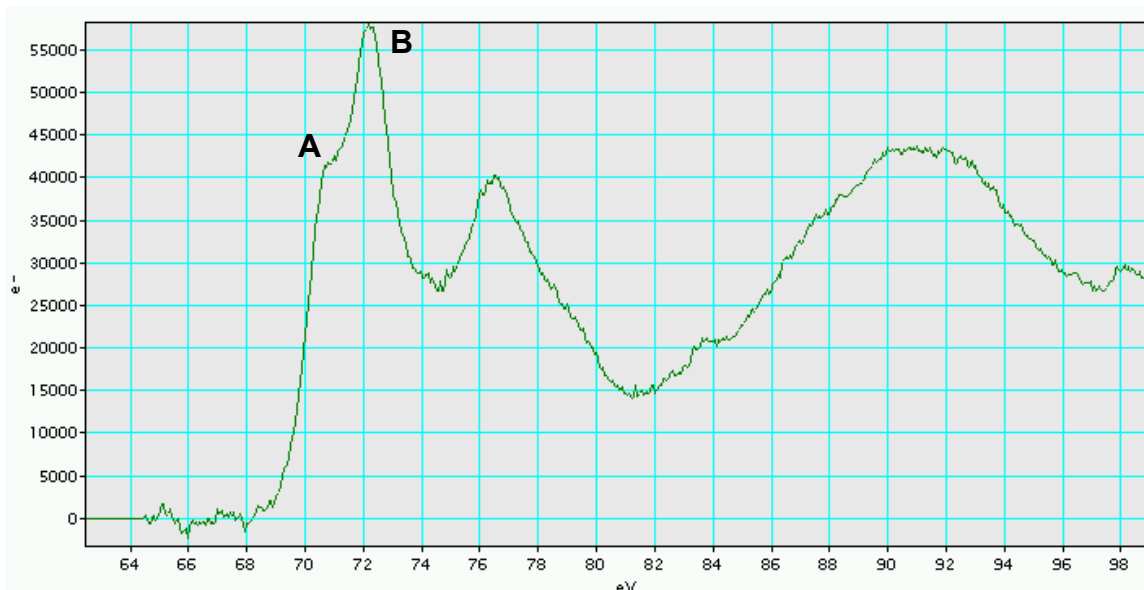

Figure 20: Aluminum peak from EELS spectra of γ-alumina taken with a 0.4 eV energy resolution.
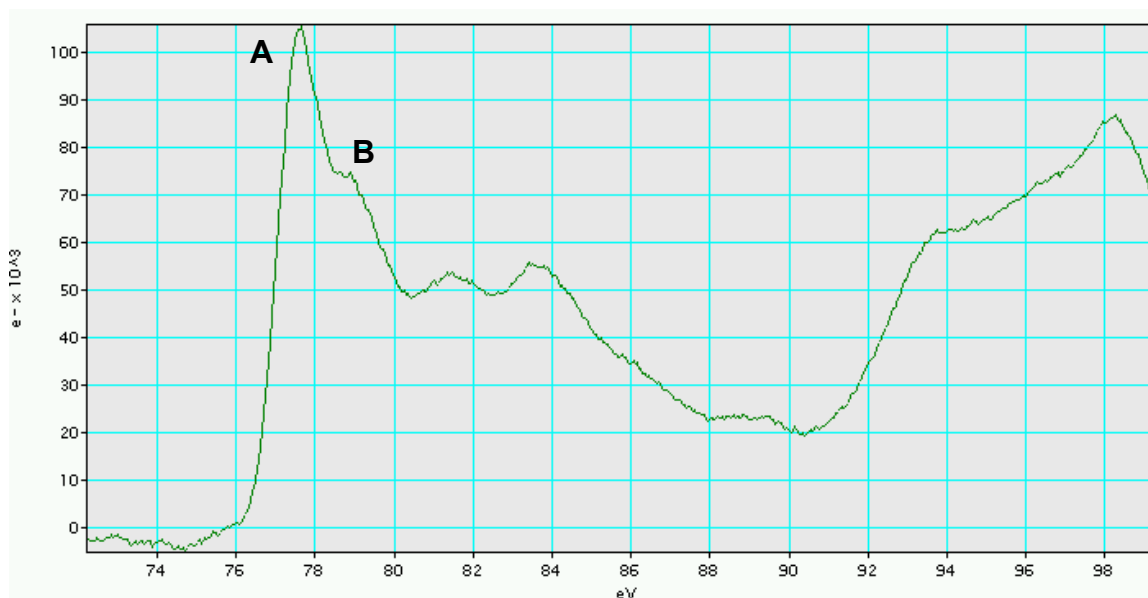
Figure 21: Aluminum peak from EELS spectra of α-alumina taken with a 0.4 eV energy resolution.

Discussion of EELS Results

The results from the electron diffraction study show the difficulty in using this method to determine the phase of nanosized crystals. Not only were some of the results inconclusive, but also very time consuming to process. Although x-ray powder diffraction results confirmed the presence of α-alumina and γ-alumina, we had no way of using the data to determine which phase was tied to which strucutre. The ease of phase identification by generating and comparing our EELS spectra to the published fingerprints shows the utility and efficiency of this method. Results came relatively quickly and were easy to interpret. Only EELS was able to unequivocably prove our suspicions that the fine powder was indeed γ-alumina and the single crystals were α-alumina. However, the published fingerprints were necessary to make this distinction. Hence, the contemorary techniques of electron diffraction and x-ray powder diffraction will continue to serve as a necessary part of futurer alumina phase studies. The previous discussion on electron diffraction should be used to facilitate future characterzation studies.

The spectra shown in Figures 20 and 21 demonstrate the functionality of running the EELS/monochromater system in STEM mode to characterize nanoparticles. Although the increased resolution did not reveal any new features in the spectra, we were able to beautifully resolve the A and B features in the first peak. Although we believe that we can better the energy resolution to 0.2 eV, we don't expect to see any new, finer features by increasing energy resolution by another 0.2 eV, as we did in this study.

Figures 22 and 23 compare our results with the published fingerprints. The two

α-alumina spectra agree very well until the transition from the second to third region.

Here the general shape of the curve is conserved, but the relative height of the peaks

begins to diverge. We see the same trend for the γ-alumina spectra shown Figure 23.

We may attribute these differences to two sources: specimen type and background noise. The published fingerprints were done on carbon vapor deposite (CVD) films, whereas we were working with nanopowder specimens. Specimen type and orientation may have some influence on the spectra, which is an anomaly we'd like to investigate in the future. However,

Figure 22: Overlaid EELS spectra of α-alumina comparing the spectrum from this study (green underlayer) with results from Larson et al (black overlayer).

the incongruencies between the spectra are more likely a result of differences in background noise. The first peak is primarily built from the interactions of electrons with the atoms in specific octahedral and tetrahedral sites. The far right peak is a combination of higher energy interactions and plasmon excitations. A plasmon is an excitied vibrational mode of the free electrons in the sample. The plasmon
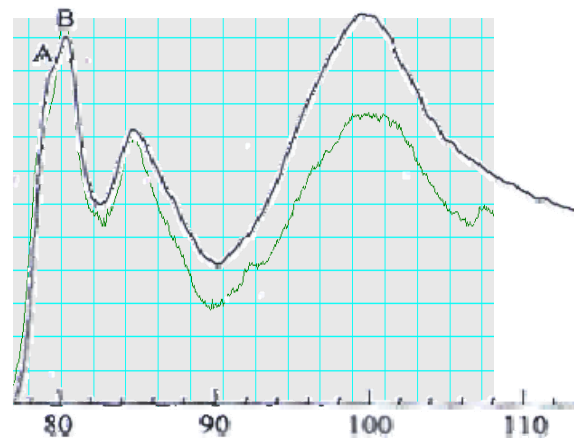
Figure 23: Overlaid EELS spectra of γ-alumina comparing the spectrum from this study (green underlayer) with results from Larson et al (black overlayer).

interaction is a much more probable process and attibutes to much of the background.

Although it occurs at lower energies, the plasmon loss can also influence the high-loss

end of the spectra if an electron is scattered multiple times. That is to say, the electron might first excite an aluminum atom then interact with the free electrons in the sample before exiting the specimen. Such a double-loss electron will contribute to the third region of the EELS spectra. As sample thickness increases, so do the number of plasmon interactions, causing a taller peak in the third region. Hence, we might conclude that the thin films used by Larson et al were thicker than the edges of the powders we were analyzing. Or, on the other hand, the difference may arise simply because of the fit used to subtract the background from the spectrum. All in all, the differences in the relative height of the first peak to the third may arise from something as simple as the type and thickness of the specimen or the fit used for the background subtraction.

We also note a difference in the relative height of the A feature in the two gamma spectrum (Figure 23). The relative location of the A and B peaks is speculated to be a function of the octahedral and tetrahedral sites. Thus, the small discrepency in Figure 23 is probably a function of the material. Observing that the A peak for our gamma spectra is lower in comparision to the spectra from the CVD films, we suggest that, due to high surface content or orientatinl differences, the electron interaction with the sites producing peak B are more preffered in our material. However, without further research into the matter, we can do little more than speculate.

Again, we note that the peaks of our spectra in Figures 20 and 21 do not fall on the same energies as published data. This axis can be calibrated using the zero-loss peak or a carbon peak. However, we were not too concerned with this aspect of the spectra since the scope of this study was more concerned with resolving the A and B features of the first peak.

Not only are we very content with the results of the investigation, but we feel we have opened the door for further research. Efforts should be made to master the nuances of the monochromator/EELS system and push forward the limits of energy resolution. A proposal was written by Dr. Vanfleet for grant money to fund a project using the polycrystalline material to explore the effect of crystal orientation on the energy spectra. With much of the work towards mastering sample preparation and understanding the crystal size and orientation of the material already accomplished, this project could very quickly produce results.

Further, we've accumulated some of the key aluminum hydroxides which will allow us to generate the other five phases of alumina. With the permission of Dr. Branton Campbell to access his high-temperature tube furnace, efforts can be made to produce and analyze these other phases, beginning with kappa. Figure 24 shows the transformation sequence of the aluminum hydroxides--of which we posses gibbsite and bayerite--to the different phases of alumina.
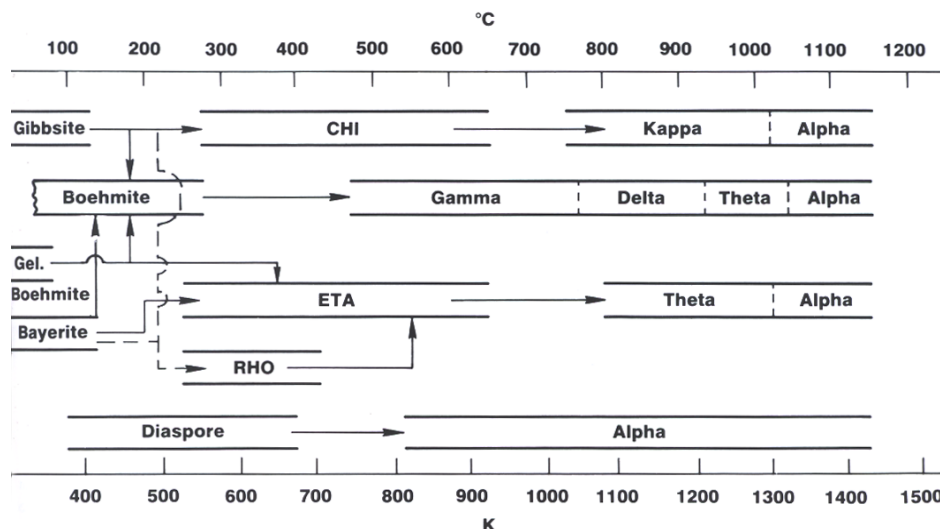
Figure 24: Transformation sequence from the aluminum hydroxides to the seven phases of alumina

Conclusion

We have succeeded in fingerprinting the gamma and alpha phases of alumina with an energy resolution of 0.4 eV. This was done by using a scanning transmission electron microscope with electron energy-loss spectroscopy and a monochromator. The analysis did not reveal any new features in the EELS spectra, but we were able to demonstrate the capability of using STEM mode to enhance definition and characterize alumina nanoparticles. While electron diffraction and x-ray powder diffraction can be used for phase identification, their results weren't as robust or conclusive as the EELS fingerprints. This exercise opens the door to future EELS research at BYU, including investigations of other alumina phases and the effect of crystal orientation on EELS spectra.

Acknowledgements

# References

[1] Wefers, K & Misra, C. (1987) <u>Oxides and Hydroxides of Aluminum</u>, Alcoa Laboratories

[2] Larsson, A., Xackrisson, J., Halvarsson, M. & Ruppi, S. (2000) <u>EELS investigation of CVD : α-Al$_2$O$_3$, κ-Al$_2$O$_3$, and γ- Al$_2$O$_3$ coatings.</u>

[3] "New Technology in the WIRE Mission" Retrieved from the World Wide wWb on January 25, 2005 from: http://sunland.gsfc.nasa.gov/smex/wire/mission/technology.html

[4] Images retrieved from the World Wide Web on March 12, 2005 from: fy.chalmers.se/~ruberto/lic.pdf

[5] Levin, I. & Brandon, D. (1998) Metastable Alumina Polymorphs: Crystal Structures and Transition Sequences. J. Am. Ceram. Soc., Vol. 81 No. 8, pp 1995-2012

[6] Mulvihill, M.L., Gulgun, M.A., Bischoff, E., and Ruhle, M., (1998) Orientation Imaging Microscopy of Alpha Alumina: Sample Preparation and Texture Analysis, *Zeitschrift fur Metallkunde,* 89:546

[7] Farrer, J.K, Michael, J.R., and Carter, C.B. (2000), EBSD of Ceramic Materials, *Electron Backscatter Diffraction in Materials Science,* A.J. Schwartz, M. Kumar and B.L. Adams, eds., Klewer Academic/Plenum Publishers, New York, N.Y., 299

[8] Carter, C.B. & Williams, D.B. (1996) <u>Transmission Electron Microscopy.</u> Plenum Press, New York, pg 150

[9] Stokes, H.T. (2000). Solid <u>State Physics for Advanced Undergraduate Students.</u> Brigham Young University, Third Edition

[10] Ahn, C.C. and Krivanek O.L. (Jan 1983) EELS Atlas, A reference guide of electron energy loss spectra covering all stable elements

[11] Stadelmann, Pierre (1998). *EMS Online: Electron Microscopy Image Simulation.* Centre Interdépartemental de Microscopie Electronique. Retrieved from the World Wide Web from: http://cimesg1.epfl.ch/CIOL/ems.html

[12] Hansen, P.L., Brydson, R., McComb, D.W., & Richardson, I. (1994) <u>EELS fingerprint of Al-coordination in silicates.</u>

[13] Egerton, R.F. (1996) <u>Electron Energy-Loss Spectroscopy in the Electron Microscope.</u> Plenum Press, New York

Appendix A

Polishing Tripod

Disc

Bar

Sample Holder

(.30)

(.50)

(⌀.25)

(⌀.50)

Feet

(.50)

(.60)

(.37)

(⌀.50)

(⌀.19)
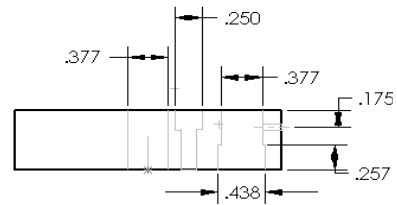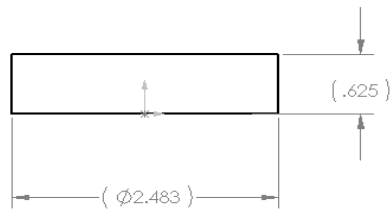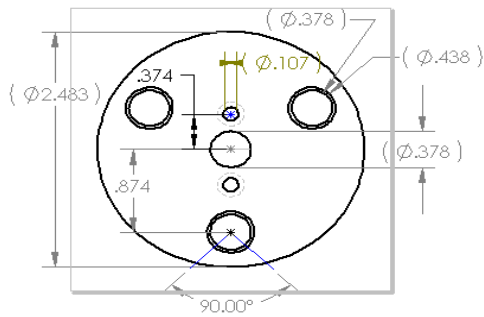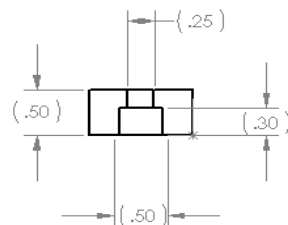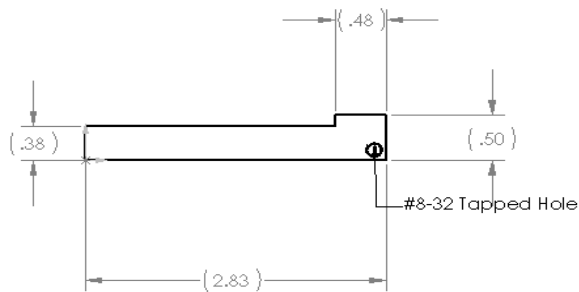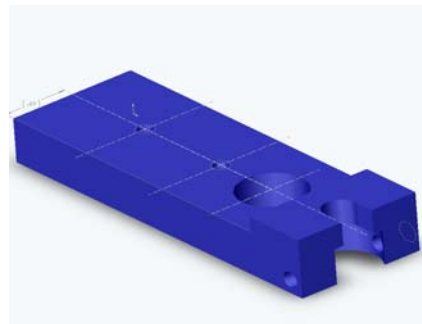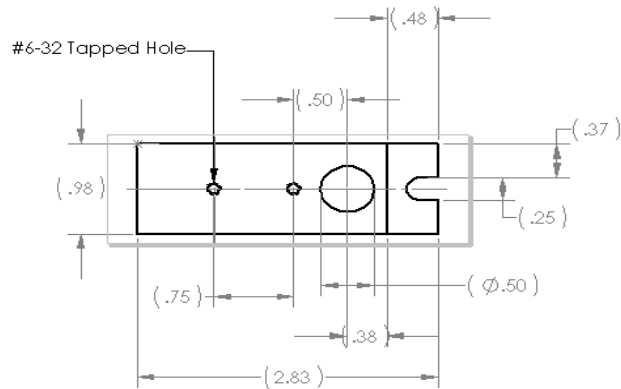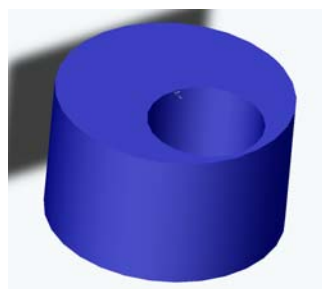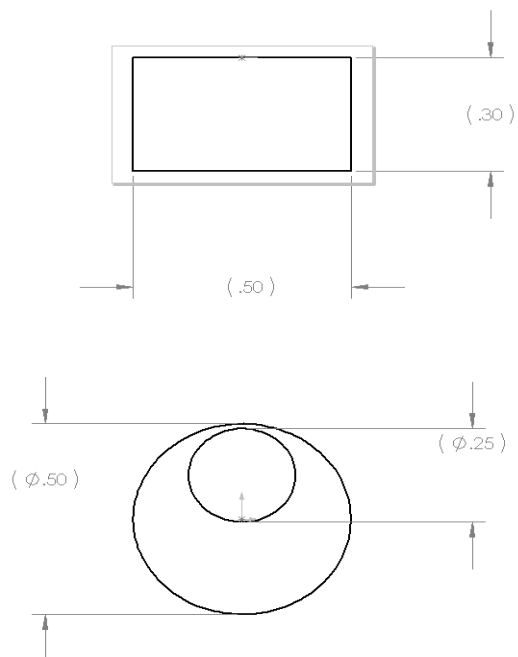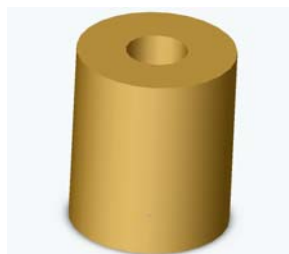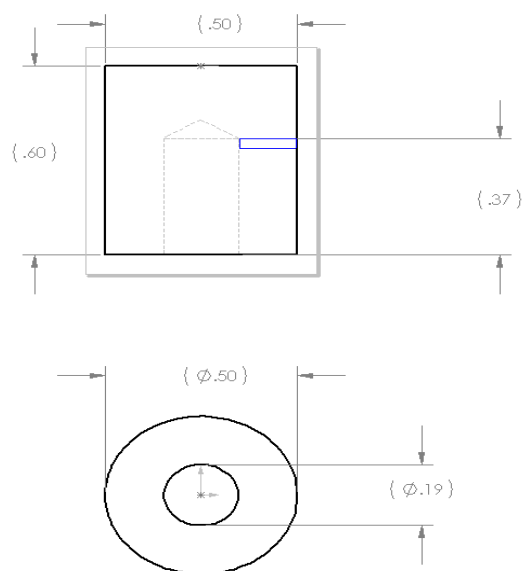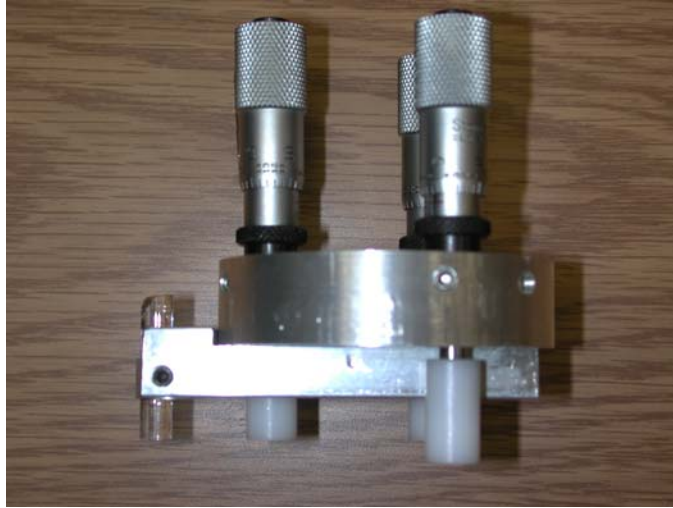
# **Polishing Tripod Machining Directions**

Main Part

1. Machine the disk to a diameter of 2.483" and thickness of .625" using the lathe.

   Note: Take care that both the two sides are perpendicular.

2. Drill the center hole and three outer holes using a V (.377") drill, making sure the relative spacing is correct and the holes are symmetric. This might be best done using an indexing head.

3. Selecting one of the outer holes, drill the two smaller holes in the appropriate locations along the diameter using a #28 drill bit.

4. Change to a .25" drill, center it over each of the smaller holes, then drill to the depth of at least .140" (this is for the screw head)

5. Flip part over, and countersink the three outer holes to a depth of .257" (not critical) using a 7/16 drill bit.

6. Flip part on end, then use the center-tap drill to start two holes at 45 degrees to the diameter around each of the three outer holes.

7. Finish these six holes with an 8-32 tap drill (#29 bit?) and thread.

Second Part

1. Cut a 0.5" by 2.83" by 0.98" rectangular block

2. From the face that is .98" wide, cut down about .12" from one end of the block to 2.35", leaving a 0.48" head.

3. With a ½" end mill drill bit, drill the two larger holes. The first is on the bottom of the part centered .15" from the edge of the block and drilled to a depth of .3" The other is drilled is centered .38" from the edge of the head of the block and goes all the way through.

4. Use the 6-32 tap drill to drill the two smaller holes in the appropriate location and thread.

5. Use a ¼" drill bit centered at the same point as the ½" drill.

6. Use the 8-32 tap drill on each side of the block

Third Part:

1. Machine a disk with a diameter of ½" and height of .3"

2. Since we have two types of glass tubing, consult the diameter of tubing you will be using to determine the width of the hole to drill.

Feet:

1. Face of the plastic

2. Drill a hole .350" deep with a #10 drill

3. Use Dr. Vanfleet's special #8 to drill the hole to a final depth of .370"

4. Cut off the piece at .6"

5. Face of the other end

6. Make a small tap into the side just above the foot hole depth